Neutron-unbound states in ^{31}Ne

D. Chrisman,[1,2,*] A. N. Kuchera,[3,†] T. Baumann,[1] A. Blake,[4] B. A. Brown,[1] J. Brown,[5] C. Cochran,[5] P. A. DeYoung,[6] J. E. Finck,[7] N. Frank,[8] P. Guèye,[1,2,4] H. Karrick,[8] H. Liu,[1,2] J. McDonaugh,[8] T. Mix,[5] B. Monteagudo,[1] T. H. Redpath,[1,9] W. F. Rogers,[10] R. Seaton-Todd,[3] A. Spyrou,[1] K. Stiefel,[1] M. Thoennessen,[1,2,‡] J. A. Tostevin,[11] and D. Votaw[1,2,§]

[1] *National Superconducting Cyclotron Laboratory, Michigan State University, East Lansing, Michigan 48824, USA*
[2] *Department of Physics and Astronomy, Michigan State University, East Lansing, Michigan 48824, USA*
[3] *Department of Physics, Davidson College, Davidson, North Carolina 28035, USA*
[4] *Hampton University, Hampton, Virginia, 23668, USA*
[5] *Wabash College, Crawfordsville, Indiana 47933, USA*
[6] *Hope College, Holland, Michigan 49423, USA*
[7] *Central Michigan University, Mt Pleasant, Michigan 48859, USA*
[8] *Department of Physics and Astronomy, Augustana College, Rock Island, Illinios 61201*
[9] *Department of Chemistry, Virginia State University, Petersburg, Virginia 23806, USA*
[10] *Indiana Wesleyan University, Marion, Indiana 46953, USA*
[11] *Department of Physics, University of Surrey, Guildford, Surrey GU2 7XH, United Kingdom*

Background: The Island of Inversion near the $N = 20$ shell gap is home to nuclei with reordered single-particle energy levels compared to the spherical shell model. Studies of ^{31}Ne have revealed that its ground state has a halo component, characterized by a valence neutron orbiting a deformed ^{30}Ne core. This lightly-bound nucleus with a separation energy of only $S_n = 170$ keV is expected to have excited states that are neutron unbound.

Purpose: The purpose of this experiment was to investigate the low-lying excited states in ^{31}Ne that decay by the emission of a single neutron.

Methods: An 89 MeV/nucleon ^{33}Mg beam impinged on a segmented Be reaction target. Neutron-unbound states in ^{31}Ne were populated via a two-proton knockout reaction. The ^{30}Ne fragment and associated neutron from the decay of ^{31}Ne were detected by the MoNA-LISA-Sweeper experimental setup at the National Superconducting Cyclotron Laboratory. Invariant mass spectroscopy was used to reconstruct the two-body decay energy ($^{30}\mathrm{Ne} + \mathrm{n}$).

Results: The two-body decay energy spectrum exhibits two features: a low-lying peak at 0.30 ± 0.17 MeV and a broad enhancement at 1.50 ± 0.33 MeV, each fit with an energy-dependent asymmetric Breit-Wigner line shape representing a resonance in the continuum. Accompanying shell model calculations using the FSU interaction within NuShellX, combined with cross-section calculations using the eikonal reaction theory, indicate that these peaks in the decay energy spectrum are caused by multiple resonant states in ^{31}Ne.

Conclusions: Excited states in ^{31}Ne were observed for the first time. Transitions from calculated shell model final states in ^{31}Ne to bound states in ^{30}Ne are in good agreement with the measured decay energy spectrum. Cross-section calculations for the two-proton knockout populating ^{31}Ne states as well as spectroscopic factors pertaining to the decay of ^{31}Ne into ^{30}Ne are used to examine the results within the context of the shell model expectations.

I. INTRODUCTION

Advances in radioactive beam facilities allow access to regions of the nuclear chart far from the valley of stability. Studies of exotic nuclei near the neutron drip line have led to the discovery of interesting structural phenomena such as the Islands of Inversion [1] in which traditional shell model gaps are diminished or shifted, and halo structures [2], described by one or more loosely bound nucleons around a deformed core, with extended nuclear radii.

One signature of a halo nucleus is the large interaction cross section, which implies an extended matter radius such as that observed in ^{11}Li [3]. Due to the centrifugal barrier, neutron-halo nuclei require s- or p-wave valence neutrons in order to account for the large observed interaction cross sections. For $N > 20$ nuclei, the spherical shell model suggests the valence neutron(s) would occupy the $f_{7/2}$ orbital; this higher angular momentum orbital is not characterized by an extended tail, implying that a halo structure in this region is indicative of level inversion with respect to the spherical shell model.

Halo structures are more common among weakly-bound neutron-rich nuclei with a handful of halo nuclei identified, ^{37}Mg being the heaviest observed [4]. According to large-basis shell model calculations, ^{31}Ne, as well as its nearest neighbors ^{30}Ne, ^{32}Ne, and ^{32}Na all belong to the $N = 20$ Island of Inversion [1].

Particle stability of ^{31}Ne was established in 1996 [5]

* Corresponding author: chrisman@nscl.msu.edu
† ankuchera@davidson.edu
‡ Present address: American Physical Society, Ridge, NY 11961, USA.
§ Present address: Los Alamos National Laboratory, Los Alamos, New Mexico 87545, USA

through a projectile fragmentation study. Neutron removal cross sections were measured at RIBF (RIKEN) by Nakamura *et al.* [6]. In this study, the authors presented reaction and large-basis shell model calculations and identified the ground state spin-parity to be $\frac{3}{2}^-$, with the halo component formed by a weakly bound p-wave neutron having about 30% of a single-nucleon strength. The significant contribution of a weakly bound low-l orbital ($l = 0$ or 1) indicates halo structure for the ^{31}Ne ground state, and by association indicates the level inversion from the independent-particle shell model ordering.

These observed changes in nuclear structure near the drip line have provided important phenomena for testing theoretical models. Studies of excited states of loosely-bound nuclei can help to provide a better understanding of the changing shell structure in exotic nuclei near the neutron drip line. Experimental information on the structure of ^{31}Ne is limited thus far to studies of the ground state, which is very weakly bound with a low, evaluated one-neutron separation energy $S_n = 170 \pm 130$ keV [7]. It is predicted that the excited states of ^{31}Ne are neutron unbound [8]. The present study aims to investigate the excited states of ^{31}Ne for the first time via the method of invariant mass spectroscopy.

II. EXPERIMENTAL SETUP

The experiment to investigate ^{31}Ne excited states took place at the National Superconducting Cyclotron Laboratory (NSCL) at Michigan State University where a 140 MeV/nucleon ^{48}Ca beam was accelerated by the K500 and K1200 coupled cyclotrons. The beam was incident on an 849 mg/cm^2 Be target to produce ^{33}Mg nuclei via projectile fragmentation. A 736 mg/cm^2 aluminum wedge was used in the A1900 fragment separator to facilitate isotopic separation of the isotope of interest, which was transported at a magnetic rigidity of 3.8 Tm to the experimental setup.

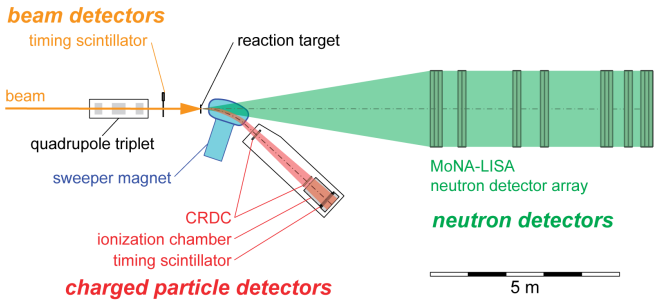

FIG. 1. (Color online) Schematic layout of the ^{33}Mg($-$2p) experiment. See text for details.

The ^{33}Mg entered the experimental hall that housed the MoNA-LISA neutron detector array [9, 10] and the large-gap superconducting Sweeper dipole magnet [11] with an energy of 88.8 ± 0.17 MeV/nucleon (see Fig. 1). The beam first passed through a 420 μm plastic timing scintillator before impinging on the segmented reaction target [12]. The latter was configured of an array of four 140 μm silicon detectors and three interleaved beryllium targets with thicknesses of 199 mg/cm^2 each.

The ^{31}Ne nuclei were produced from a ^{33}Mg($-$2p) knockout reaction in one of the three Be targets. The ^{31}Ne nuclei produced may have populated the bound ground state or neutron-unbound excited states that decay immediately into a ^{30}Ne fragment and a neutron. The ^{30}Ne fragment was centered on the face of the first of two Cathode Readout Drift Chambers (CRDCs) after travelling through the large-gap (14 cm) "Sweeper" superconducting dipole magnet [11]. The neutron associated with the decay was detected in one of the 10 cm $\times$ 10 cm $\times$ 200 cm bars from the MoNA-LISA plastic scintillator array [9, 10]. The position and energy loss of the ^{30}Ne charged fragment were measured using the two CRDCs and an ionization chamber, respectively. The fragment time of flight was measured using a plastic scintillator at the target position and another at the end of the charged particle detector setup. The position and time-of-flight of the forward moving neutrons were measured in coincidence within an accuracy of ~ 7 cm and 100 ps, respectively.

III. ANALYSIS

The time of flight of all the fragments (e.g., secondary beams) transmitted to the experimental hall were measured from the A1900 fragment separator focal plane to the target position. This information can be used in combination with the energy loss measured in the first Si detector of the segmented target to create a particle identification plot for the incoming beams. The ^{33}Mg isotope is selected by placing appropriate gates on these parameters.

The charged ^{30}Ne fragments were detected and subsequently identified using a suite of charged particle detectors following the Sweeper magnet. An element identification can be made based on the energy loss in the ionization chamber and the time of flight between two plastic timing detectors located just upstream from the reaction target and at the end of the Sweeper charged particle detectors, as illustrated in Fig. 1.

After isolating the events corresponding to $Z = 10$, an identification of mass number A is required to select the desired ^{30}Ne isotope. This identification is achieved by a combination of the flight time, position, and angle measurements. A neutron hit is then required in coincidence with the ^{30}Ne fragment to ensure that these events are attributed to the decay of an unbound excited state of ^{31}Ne.

The two-body decay energy is reconstructed from the measured four-momenta of the decay products of ^{31}Ne* (*i.e.*, ^{30}Ne + n) using the invariant mass technique. Reconstructing the four-momentum for the neutron at the

target is straightforward using time of flight and position. For the charged fragment, the measured positions and angles in the charged particle detectors are used with a third-order ion-optical matrix transformation to determine the angles and positions of the charged fragments at the reaction target. The ion-optical matrix was calculated from the magnetic field map using COSY INFINITY [13]. It is assumed that the two-proton knockout and the neutron emission happen at the mid point of one of the three beryllium targets and the appropriate energy is added back to account for the energy loss of the exiting charged reaction product. The segmented target allows one to properly identify the target segment where the reaction took place [12], and subsequently the added back energy specific to where the two-proton knockout process took place.

Monte Carlo simulations that include the experimental setup and energy-dependent Breit-Wigner line shapes with theoretical decay energy distributions (including decay modes and reaction mechanisms), beam parameters, and the Sweeper magnetic field as well as the detector acceptances, efficiencies and resolutions were performed. These simulated data sets are directly compared to the experimental data. The neutron interactions were simulated using the Geant4 Monte Carlo toolkit [14, 15] with the physics class of MENATE_R [16]. The simulations were benchmarked against several experimentally reconstructed observables, *i.e.* positions, kinetic energies, and relative velocities.

IV. RESULTS AND DISCUSSION

The experimentally reconstructed two-body decay energy spectrum for ^{31}Ne* is shown in Fig. 2. The simulation assumes that the emitted decay products are isotropic in the center-of-mass frame and a weighted log likelihood fit is used to extract the resonance parameters represented by asymmetric Breit-Wigner line shapes.

Two resonant line shapes at minimum are needed to describe the shape of the two-body decay energy spectrum. The fit using two resonances results in decay energies of 0.30 ± 0.17 MeV and 1.50 ± 0.33 MeV.

The uncertainties quoted represent the uncertainties of the log likelihood fit and include the detector resolutions and acceptance of the experimental setup. The energy resolutions of the experimental setup at these energies are roughly 150 keV and 370 keV respectively.

The two-proton removal cross sections populating the negative parity ^{31}Ne(J^{π}) final states, at 88.8 MeV/nucleon on a ^{9}Be target, are calculated using the eikonal, direct reaction model approach of Ref. [17]. The ground-state to ground-state two-proton separation energy is 40.80 MeV [18], driving the direct nature of the 2p reaction mechanism [19]. Both, the $\langle 2\mathrm{p}, ^{31}\mathrm{Ne}(J^{\pi})|^{33}\mathrm{Mg}(3/2^{-})\rangle$ overlaps that generate the Two-Nucleon Amplitudes (TNAs) of the removed *sd*-shell protons, and the spectrum of unbound excited ^{31}Ne final states are taken from the FSU interaction [20] shell-model calculations made using the code NUSHELLX [21]. The FSU Hamiltonian uses the sd-pf model space with the constraint that the protons are in the *sd* shell. The neutron configuration for ^{33}Mg and ^{31}Ne is $(sd)^{(-2)}(fp)^{3}$, and the neutron configuration for ^{30}Ne is $(sd)^{(-2)}(fp)^{2}$. Hartree-Fock calculations were used to constrain both, the density of the ^{31}Ne residues for the calculation of the residue-target interaction, and the geometry parameters of the real Woods-Saxon potentials used to bind the single-particle orbitals of the removed protons. This follows the method discussed in Ref. [22]. Analogous shell-model calculations are used to compute the $\langle \mathrm{n}, ^{30}\mathrm{Ne}(J^{\pi}_{f})|^{31}\mathrm{Ne}(J^{\pi})\rangle$ overlaps and spectroscopic factors for the neutron decays of the particle-unbound final states.

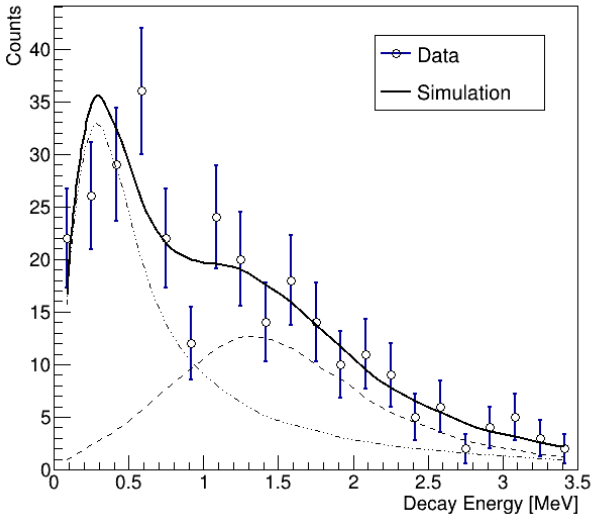

FIG. 2. (Color online) Two-body decay energy spectrum of ^{31}Ne*. Data is represented by the open circles and the sum of the simulated resonances by a solid black line. The dotted dashed line and dashed line are the individual asymmetric Breit-Wigner resonant line shapes, which have been subjected to acceptance and efficiency effects.

The two-proton knockout cross sections to the first 30 negative-parity states of each spin are shown in Fig. 3. A summary of the more strongly populated levels and their cross sections that include spectroscopic factors can be seen in Table I. Only levels in ^{31}Ne with a cross section for the one neutron decay to ^{30}Ne + n larger than 0.020 mb are shown. A level scheme based on experimental data and levels from shell model calculations can be seen in Fig. 4. The two extracted decay energies from the fit to data are color coded in the figure: red (300 keV) and blue (1.50 MeV). Due to the absence of gamma-ray detection, decays to excited states in ^{30}Ne cannot be discriminated but must be considered. The color-coded lines in the center column illustrate possible levels based on decays to accessible states in the daughter nucleus ^{30}Ne.

For example, the red lines are located 300 keV above each ^{30}Ne level.

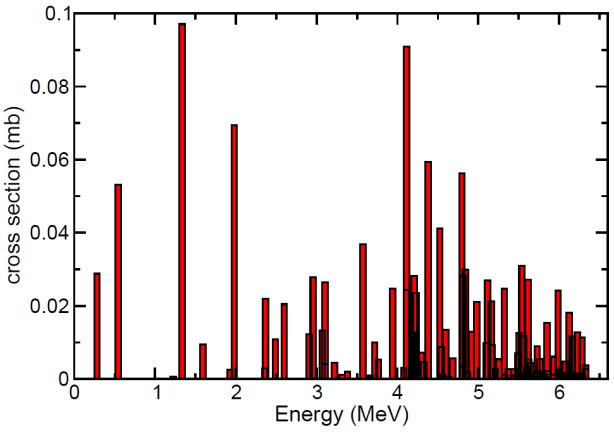

FIG. 3. (Color online) Two-proton knockout cross sections to the first 30 negative parity unbound states of each spin as a function of the ^{31}Ne* energy above threshold.

TABLE I. Calculated cross sections (σ) for the ^{33}Mg($-$2p)^{31}Ne and ^{31}Ne* $\rightarrow$ ^{30}Ne + n decays. This cross-section folds in spectroscopic factors pertaining to a specific decay. E_x is the energy of the ^{31}Ne level, $E_{\rm n}$ is decay energy and Γ_t is the decay width for each of the spin parity states J^π.

$2J^\pi$	E_x (MeV)	σ (mb)	J_f^π	$E_{\rm n}$ (MeV)	Γ_t (MeV)
5^-	0.43	0.029	0^+	0.26	0.004
7^-	0.70	0.053	0^+	0.53	0.157
9^-	1.49	0.097	2^+	0.52	0.167
11^-	2.13	0.069	2^+	1.17	0.367
7^-	2.52	0.022	2^+	1.56	0.541
5^-	3.11	0.027	2^+	2.15	0.698
7^-	3.72	0.032	4^+	1.32	0.423
7^-	4.27	0.086	4^+	1.86	0.464
7^-	4.36	0.022	4^+	1.95	0.275
5^-	4.53	0.027	2^+	2.13	0.468
	4.53	0.027	4^+	3.57	0.468
7^-	4.95	0.054	4^+	2.54	0.129
11^-	4.99	0.023	4^+	2.59	0.215

The measured two-body decay energy represents the energy released when a neutron-unbound excited state of ^{31}Ne decays to a state in ^{30}Ne. Determining the energy of a potentially observed level in ^{31}Ne relative to its ground state requires knowledge of the one-neutron separation energy, which at present has a large uncertainty, at $S_n = 170 \pm 130$ keV [7]. Potential decay paths from ^{31}Ne considered include a decay to either the ground state of ^{30}Ne, the 2^+ state at 0.79 MeV, or the 4^+ state at 2.23 MeV [23].

The fit to the decay energy spectrum considers two resonances, which is the minimum needed to describe the overall shape of the measured spectrum. However, shell model calculations predict multiple strong decays that could possibly be observed with improved resolution. See Table I for details on the decays discussed below.

The first feature of the two-body decay energy is a low-lying peak, fit with a resonant line shape at $E_{\rm n} = 0.30 \pm 0.17$ MeV. The log likelihood is not sensitive to the width of the line shape but indicates it is broader than the experimental resolution. The likelihood indicates a width of at least 1 MeV is needed to fit the decay energy spectrum. The shell model predicts three states with associated decay energies consistent with this measurement. The $\frac{9}{2}^-$ state at 1.49 MeV has the largest cross section from the two-proton knockout at 0.097 mb and the decay to the 2^+ state in ^{30}Ne would give an $E_{\rm n}$ of 0.52 MeV. The $\frac{7}{2}^-$ state at 0.70 MeV has a cross section of 0.053 mb and a decay to the ground state of ^{30}Ne would result in an $E_{\rm n}$ of 0.53 MeV. These two decays are close in energy, but populate different daughter states in ^{30}Ne. The absence of gamma ray detection in our setup means these two decays cannot be resolved. A third decay consistent with this energy is of the first excited state of ^{31}Ne, with a spin-parity of $\frac{5}{2}^-$ at 0.43 MeV, decaying to the ground state of ^{30}Ne, with a decay energy of 0.26 MeV. The widths of these individual decays are narrow (less than 200 keV, see Table I). The large width of the fit used to describe this feature of the spectrum strengthens the interpretation as a group of unresolved resonances.

The second resonance in the maximum likelihood fit is at $E_{\rm n} = 1.50 \pm 0.33$ MeV above the neutron threshold. There are multiple calculated decays that are consistent with this measurement. The $\frac{11}{2}^-$ at 2.13 MeV decaying to the 2^+ state in ^{30}Ne is predicted to be a prominent decay with an $E_{\rm n}$ of 1.17 MeV. Also consistent with this measurement is another prominent decay of the $\frac{7}{2}^-$ state at 3.72 MeV to the 4^+ state of ^{30}Ne with an $E_{\rm n}$ of 1.32 MeV. It is also worth noting that although the decay from the first $\frac{9}{2}^-$ state in ^{31}Ne decaying to the ground state of ^{30}Ne is consistent with this measured decay energy (see Fig. 4), it is outside the model space of the shell model calculations performed. The single-particle decay width for an $l = 5$ decay is about 0.026 keV. The spectroscopic factor for mixing an $h_{9/2}$ orbital about 30 MeV above the $0f_{7/2}$ must be less than about 0.01. This indicates a width for the decay to 0^+ being less than 0.26 eV; which is not expected to compete with the decay to 2^+ which has a decay width of 0.167 MeV (see Table I).

The shell model calculations listed in Table I are a subset of the calculated decays with two-proton knockout cross sections greater than 0.02 mb. Figure 3 shows the cross section calculations have considerable relative strength up to 6.5 MeV, resulting in a large number of possible decays. When the various decays to daughter states in ^{30}Ne are calculated for states with cross sections down to 0.001 mb, there are 140 total decays to consider. Figure 5 shows a comparison of shell model

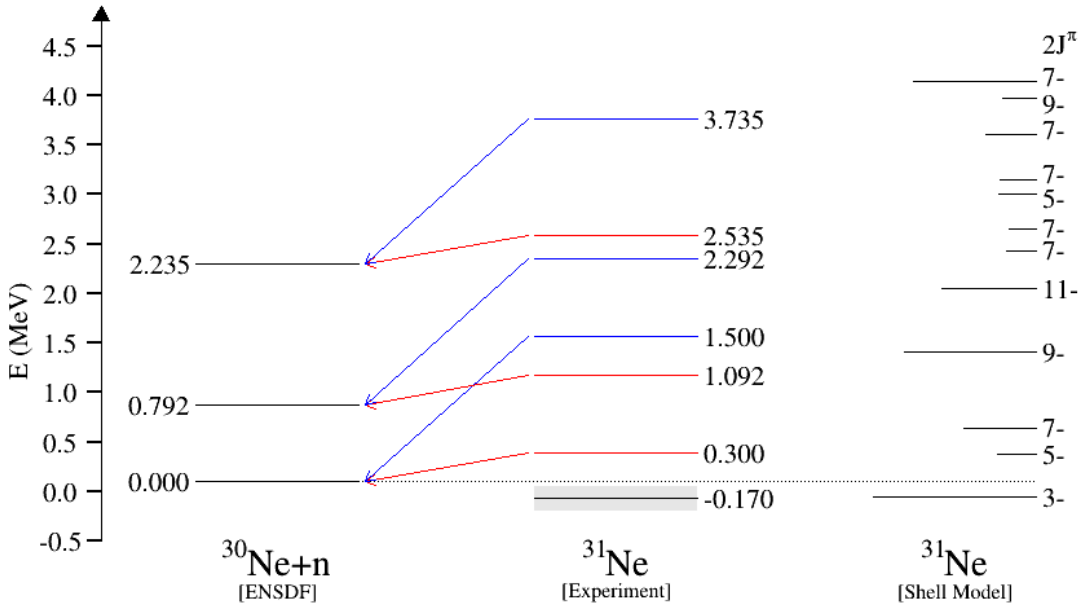

FIG. 4. (Color online) Decay energy and level scheme for the decay of ^{31}Ne into ^{30}Ne + n. In the center are levels potentially observed by the present experiment, color coded by the measured decay energies (see text for detail). The arrows specify potential decay paths to states in ^{30}Ne with colors indicating the measured decay energies. The right spectrum shows the NuShellX calculations. The length of the bars (excluding the ground state) indicate a population cross section from the two-proton knockout. Energies listed are relative to the one-neutron separation energy of ^{31}Ne.

theory to the measured data. The top line indicates a one neutron decay for all calculated ^{31}Ne states. The bottom line includes only the decays from ^{31}Ne states below S_{2n} = 3.72 MeV [24]. The shaded area is a difference between these two assumptions: either all ^{31}Ne states decay via one neutron decay, or only states below S_{2n} decay via one neutron decay. In reality, these processes compete and an accurate picture of this complex decay spectrum lies in between the two. The shape of the measured data spectrum is not inconsistent with the predictions of the shell model calculations.

V. SUMMARY AND OUTLOOK

This experiment aimed to study the excited states of ^{31}Ne for the first time, and the results are interpreted in the context of shell model calculations. ^{31}Ne is a prime example of a halo nucleus in the Island of Inversion and can give insight into other nuclei in this region.

The neutron decay calculations performed indicate a complex scenario. Calculating the two-proton knockout cross sections up to roughly 6.5 MeV gives more than 100 potential decays to consider. The experimentally measured decay energy spectrum can be fit with two resonant line shapes, interpreted here as collections of relatively strong narrower decays. The neutron decay calculations show that the neutron decay spectrum is composed of many unresolved peaks, the shape of which is not inconsistent with the observed spectrum.

To get a better understanding of how ^{31}Ne is related to other neutron-rich nuclei in the same region, further studies attempting to resolve the various resonances would be useful. The addition of gamma ray detection in a future MoNA-LISA experiment would be well-suited to clarify the observation of specific energy levels in ^{31}Ne and give a better understanding of the shell evolution in the region of the $N = 20$ Island of Inversion.

ACKNOWLEDGMENTS

We would like to acknowledge the effort of the National Superconducting Cyclotron Laboratory operations staff for providing high-quality beams and device support for the Sweeper detectors. We would also like to acknowledge the MoNA collaboration for providing device support for MoNA-LISA and Sweeper detectors and contributions to the experiment execution. This work was supported by the National Science Foundation, USA under Grants

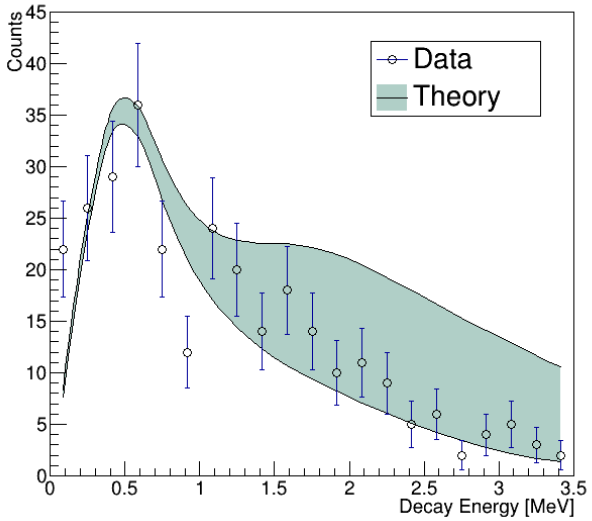

FIG. 5. (Color online) Solid lines represent theoretical decay energy spectra. The larger distribution (top line) assumes one neutron decay for all calculated ^{31}Ne states. The smaller distribution (bottom line) includes decays only from states in ^{31}Ne below $S_{2n} = 3.72$ MeV. The markers indicate the measured spectrum. The only free parameter for this comparison is the overall scaling.

No. PHY-1102511, PHY-1565546, PHY-1613188, PHY-1713522, PHY-1613429, PHY-1713956, PHY-1205357, PHY-2011398 and PHY-2012040. This work was also supported by the Department of Energy National Nuclear Security Administration, USA through the Nuclear Science and Security Consortium under Award No. DE-NA0003180 and/or DE-NA0000979. J.A.T. acknowledges support from the Science and Technology Facilities Council (UK) Grant No. ST/L005743/1.

[1] E. K. Warburton, J. A. Becker, and B. A. Brown, Phys. Rev. C **41**, 1147 (1990).
[2] I. Tanihata, J. Phys. G: Nuc. Part. Phys. **22** (1996).
[3] I. Tanihata, H. Hamagaki, O. Hashimoto, Y. Shida, N. Yoshikawa, K. Sugimoto, O. Yamakawa, T. Kobayashi, and N. Takahashi, Phys. Rev. Lett. **55**, 2676 (1985).
[4] N. Kobayashi *et al.*, Phys. Rev. Lett. **112**, 242501 (2014).
[5] H. Sakurai *et al.*, Phys. Rev. C **54**, R2802 (1996).
[6] T. Nakamura *et al.*, Phys. Rev. Lett. **112**, 142501 (2014).
[7] M. Wang, W. Huang, F. Kondev, G. Audi, and S. Naimi, Chinese Physics C **45**, 030003 (2021).
[8] P. Descouvemont, Nuclear Physics A **655**, 440 (1999).
[9] B. Luther *et al.*, Nuclear Instruments and Methods in Physics Research Section A: Accelerators, Spectrometers, Detectors and Associated Equipment **505**, 33 (2003), Proceedings of the tenth Symposium on Radiation Measurements and Applications.
[10] T. Baumann *et al.*, Nuclear Instruments and Methods in Physics Research Section A: Accelerators, Spectrometers, Detectors and Associated Equipment **543**, 517 (2005).
[11] M. D. Bird, S. J. Kenney, J. Toth, H. W. Weijers, J. C. DeKamp, M. Thoennessen, and A. F. Zeller, IEEE Transactions on Applied Superconductivity **15**, 1252 (2005).
[12] T. Redpath *et al.*, Nuclear Instruments and Methods in Physics A. **977** (2020).
[13] K. Makino and M. Berz, Nuclear Instruments and Methods in Physics Research Section A: Accelerators, Spectrometers, Detectors and Associated Equipment **558**, 346 (2006), Proceedings of the 8th International Computational Accelerator Physics Conference.
[14] S. Agostinelli *et al.*, Nuclear Instruments and Methods in Physics Research Section A: Accelerators, Spectrometers, Detectors and Associated Equipment **506**, 250 (2003).
[15] J. Allison *et al.*, IEEE Transactions on Nuclear Science **53**, 270 (2006).
[16] B. Roeder, EURISOL Design Study, Report:[10-25-2008-006-In-beamvalidations. pdf, pp 31-44] (2008).
[17] J. A. Tostevin and B. A. Brown, Phys. Rev. C **74**, 064604 (2006).
[18] W. Huang, G. Audi, M. Wang, F. G. Kondev, S. Naimi, and X. Xu, Chinese Physics C **41**, 030002 (2017).
[19] J. A. Tostevin, G. Podolyák, B. A. Brown, and P. G. Hansen, Phys. Rev. C **70**, 064602 (2004).
[20] R. S. Lubna, K. Kravvaris, S. L. Tabor, V. Tripathi, E. Rubino, and A. Volya, Phys. Rev. Research **2**, 043342 (2020).
[21] B. Brown and W. Rae, Nuclear Data Sheets **120**, 115 (2014).
[22] A. Gade *et al.*, Phys. Rev. C **77**, 044306 (2008).
[23] P. Fallon *et al.*, Phys. Rev. C **81**, 041302 (2010).
[24] M. Wang, G. Audi, A. H. Wapstra, F. G. Kondev, M. MacCormick, X. Xu, and B. Pfeiffer, Chin.Phys.C **36**, 1603 (2012).